Dark-bright excitons mixing in alloyed InGaAs self-assembled quantum dots

Michał Zieliński*

Institute of Physics, Faculty of Physics, Astronomy and Informatics and Nicolaus Copernicus University, ul. Grudziądzka 5, 87-100 Toruń, Poland

(Received 23 December 2020; revised 26 March 2021; accepted 30 March 2021; published 20 April 2021)

Quantum dots are arguably one of the best platforms for optically accessible spin-based qubits. The paramount demand of extended qubit storage time can be met by using a quantum-dot-confined dark exciton: a long-lived electron-hole pair with parallel spins. Despite its name, the dark exciton reveals weak luminescence that can be directly measured. The origins of this optical activity remain largely unexplored. In this work, using the atomistic tight-binding method combined with the configuration-interaction approach, we demonstrate that atomic-scale randomness strongly affects the oscillator strength of dark excitons confined in self-assembled cylindrical InGaAs quantum dots with no need for faceting or shape-elongation. We show that this process is mediated by two mechanisms: mixing dark and bright configurations by exchange interaction, and the equally important appearance of nonvanishing optical transition matrix elements that otherwise correspond to nominally forbidden transitions in a nonalloyed case. The alloy randomness has an essential impact on both bright and dark exciton states, including their energy, emission intensity, and polarization angle. We conclude that, due to the atomic-scale alloy randomness, finding dots with the desired dark exciton properties may require exploration of a large ensemble, similarly to how dots with low bright exciton splitting are selected for entanglement generation.

DOI: 10.1103/PhysRevB.103.155418

I. INTRODUCTION

The optically weakly active [1–5] exciton states confined in quantum dots [6,7], also known as dark excitons (DEs) [8], are promising candidates for applications in quantum information processing [2,4,9–12]. Together with optically active bright excitons (BEs), electron-hole pairs with opposite spins far better studied for, e.g., entanglement generation [13–16], they may form important building blocks for future quantum devices. However, this applicability is strongly dependent on the ability to understand and control the details of excitonic spectra, so-called "excitonic fine structure" [8]. On the one hand, the bright exciton spectrum is determined largely by quantum-dot symmetry properties [17–28], with extensive efforts [29–42] aimed at reduction of the bright exciton splitting (BES). On the other hand, the dark exciton fine structure has been studied to a far lesser degree. In particular, contrary to simplified theoretical predictions [8], the dark exciton can gain a non-negligible optical activity, even without an external magnetic field [18,21], whereas the origins of this luminescence remain largely unexplored [43,44].

Accurate theoretical modeling of excitonic fine structure, regarding both bright and dark excitons, still presents a serious challenge for approaches utilizing continuum-media approximation [18,45,46], and even for atomistic methods [10,21,47]. In this work, we use a combination of tight-binding (TB) and configuration-interaction (CI) methods, which proved its ability to find excitonic fine structure in good agreement with experiment [21,48,49]. To understand the role of disorder due to alloy randomness, we present an extensive theoretical study of the properties of bright and dark excitons calculated for an ensemble of 300 alloyed $In_{0.5}Ga_{0.5}As$ self-assembled quantum dots, each treated with the same atomistic resolution.

We find that alloy randomness, by reducing the overall symmetry, leads to (i) nonvanishing matrix elements of the optical transition (optical/transition dipole moments), as well as (ii) non-negligible exchange integrals mixing bright and dark excitonic configurations. There are thus two equally important sources of nonzero oscillator strength for the in-plane dark excitonic emission. On the contrary, the out-of-plane (z) polarized emission is dominated by the contribution from the matrix element of the optical transition only, which is in turn governed by the valence-band mixing, in agreement with the phenomenological understating of dark exciton states. Therefore, contrary to the case of in-plane emission, the exchange mixing does not play a role for z-polarized dark exciton emission.

While most of the quantum dots in ensembles reveal rather weak dark exciton activity, we show that a mere alloy randomness triggers the dark exciton optical activity reaching up to a fraction of $1/6000$ of that for the bright exciton, without faceting or shape elongation [3,10,44]. This conclusion is valid for both out-of-plane and in-plane polarizations. As the optical activity of a dark exciton is inversely proportional to its lifetime, a strong variation of the former translates to a pronounced dot-to-dot variation of the latter on a millisecond scale, while the bright exciton lifetimes tend to be systematically close to 1 ns. Moreover, despite the overall cylindrical quantum-dot shape, and despite strong alloying, the polarization properties of both bright and dark excitons for in-plane emission reveal hallmarks of a pronounced anisotropy due to the underlying crystal lattice.

*mzielin@fizyka.umk.pl

The paper is organized as follows: after a short theoretical introduction in Sec. II, we start with a discussion of bright exciton spectra and polarization angles in Sec. III. Throughout most of the paper, we aim to bridge between atomistic results and the effective treatment based on valence-band mixing. When feasible, these discussions are augmented with an abridged statistical analysis. In Sec. IV, we study in-plane emission from dark excitons, including their polarization properties, and finally we study excitonic lifetimes in Sec. V.

II. SYSTEMS AND METHODS

The calculation starts with finding atomic positions that minimize the total elastic energy by using the valence force field (VFF) method of Keating [50,51]. Minimization of strain energy is performed with the conjugate gradient method [52,53]. Next, the piezoelectric potential [54–59] is calculated by accounting for both linear and quadratic contributions, with piezoelectric coefficients from Ref. [56]. The single-particle spectra of electrons and holes are obtained with the empirical $sp^3d^5s^*$ tight-binding method accounting for d-orbitals and spin-orbit interaction [49,60–62]. The tight-binding calculation is performed on a smaller domain than the valence force field calculation [63,64]. The details regarding the $sp^3d^5s^\star$ tight-binding calculations for various nanostructures are discussed thoroughly in our earlier papers [49,52,62,65,66].

We note that eigenstates of the tight-binding Hamiltonian are doubly degenerate due to time-reversal-symmetry [67]. Therefore, for convenience, in several places we label tight-binding electron ground states with up and down spin-indices, i.e., $e_\uparrow$ and $e_\downarrow$. However, we emphasize that due to spin-orbit interaction and low overall symmetry, due to the underlying lattice with alloying, the spin in no longer a good quantum number, and such labeling is only approximate. Similarly, we label atomistically obtained hole ground states with double-arrows, i.e., $h_\Uparrow$ and $h_\Downarrow$, even though due to valence-band mixing and alloying they do not exactly correspond to heavy-hole $\pm\frac{3}{2}$ eigenstates.

After the tight-binding stage of calculations, the excitonic spectra [68] are calculated with the configuration-interaction method described in detail in Ref. [65]. The Hamiltonian for the interacting electron-hole pair can be written in second quantization as follows [68]:

$$\hat{H}_{\rm ex} = \sum_i E_i^e c_i^\dagger c_i + \sum_i E_i^h h_i^\dagger h_i \;- \sum_{ijkl} V_{ijkl}^{eh,{\rm dir}} c_i^\dagger h_j^\dagger h_k c_l + \sum_{ijkl} V_{ijkl}^{eh,{\rm exch}} c_i^\dagger h_j^\dagger c_k h_l, \tag{1}$$

where E_i^e and E_i^h are the single-particle electron and hole energies obtained at the single-particle stage of calculations, respectively, and V_{ijkl} are Coulomb matrix elements (Coulomb direct and exchange integrals) calculated according to the procedure given in Ref. [65]. More details regarding the Coulomb matrix element computation for tight-binding wave functions can also be found in Refs. [69,70] as well as in our recent papers [71,72].

Finally, the optical spectra are found by calculating the intensity of photoluminescence from the recombination of an electron-hole pair using Fermi's golden rule,

$$I(\omega) = \left|\sum_{c,v} C_{c,v}^i \langle\Psi_c|\vec{\boldsymbol{\epsilon}}\cdot\vec{\boldsymbol{r}}|\Psi_v\rangle\right|^2 \delta(E_i-\hbar\omega) = \left|\sum_{c,v} C_{c,v}^i M_{c,v}^{\vec{\boldsymbol{\epsilon}}}\right|^2 \delta(E_i-\hbar\omega), \tag{2}$$

where E_i is the energy of the initial ith state of the exciton, $C_{v,c}^i$ are CI expansion coefficients for the ith state obtained by solving Eq. (1), and $M_{c,v}^{\vec{\boldsymbol{\epsilon}}} \equiv \langle\Psi_c|\vec{\boldsymbol{\epsilon}}\cdot\vec{\boldsymbol{r}}|\Psi_v\rangle$ is the optical dipole moment matrix element calculated from single-particle tight-binding electron Ψ_c and hole Ψ_h wave functions, respectively, for a given polarization of light $\vec{\boldsymbol{\epsilon}}$, e.g., $M_{e_\uparrow,h_\Downarrow}^z = \langle e_\uparrow|z|h_\Downarrow\rangle$ for z-polarized (out-of-plane) light, and the optical (transition) dipole matrix element involving ground electron and hole states with opposite (quasi)spins.

Fermi's golden rule allows for a calculation of the first-order radiative recombination lifetime in a similar manner [73–75],

$$\frac{1}{\tau_i} = \frac{4n\alpha\omega_i^3}{3c^2} \sum_{\vec{\boldsymbol{\epsilon}}=\vec{\boldsymbol{x}},\vec{\boldsymbol{y}},\vec{\boldsymbol{z}}} \left|\sum_{c,v} C_{c,v}^i M_{c,v}^{\vec{\boldsymbol{\epsilon}}}\right|^2, \tag{3}$$

where $\omega_i = E_i/\hbar$, $n = 3.6$ [73] is the refractive index, α is the fine-structure constant, c is the speed of light in the vacuum, x, y are the in-plane radiative decay channel, and z is the out-of-plane radiative decay channel. Finally, the average bright exciton radiative lifetime, assuming identical occupation of two bright exciton states BE1 and BE2 (discussed later in the text), and neglecting thermal effects, is calculated as [74,75]

$$\frac{1}{\tau_{\rm BE}} \approx \frac{1}{2}\left(\frac{1}{\tau_{\rm BE1}} + \frac{1}{\tau_{\rm BE2}}\right) \tag{4}$$

with an analogous formula for the dark exciton.

Using the above formalism, we perform calculations for an ensemble of alloyed $In_{0.5}Ga_{0.5}As$ lens-shaped quantum dots located on a wetting layer (Fig. 1), with low overall (shape + alloyed lattice) C_1 symmetry. Each quantum-dot system is treated separately by the full VFF/TB/CI calculation. The height of all quantum dots is equal to 3 nm, whereas the

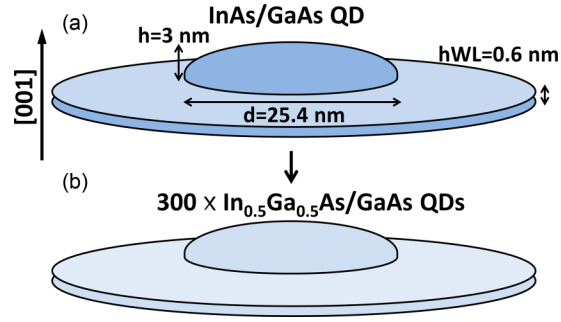

FIG. 1. Schematics of systems under consideration: (a) a lens-shaped InAs/GaAs self-assembled quantum dot located on a wetting layer, and (b) alloyed $In_{0.5}Ga_{0.5}As$ quantum dots with the same dimensions, however with 300 randomly generated samples (realizations) corresponding to the same average composition, yet a different (random) atomic arrangement. See the text for details. Surrounding GaAs material is not shown.

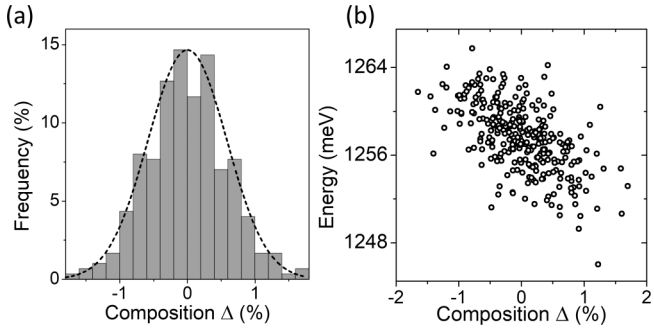

FIG. 2. (a) Histogram illustrating the distribution of average composition variations (from ideal 50% gallium content) for a family of 300 alloyed quantum dots studied in the text; (b) exciton ground-state energy as a function of composition difference and alloy randomness. See the text for details.

diameter is 25.4 nm. Each quantum dot is located on a 0.6-nm-thick (one lattice constant) wetting layer. A quantum-dot system with such dimensions (in particular in a nonalloyed InAs/GaAs variant) has been studied thoroughly in the literature (including our own work [49,62]) as a model of a typical self-assembled quantum dot. For comparison, in several places we discuss also results obtained for a C_{2v} InAs quantum dot, with no gallium admixture (no alloying; upper part of Fig. 1). However, our focus is on the alloyed system by considering 50% admixture of the barrier material in the dot region, i.e., an $In_{0.5}Ga_{0.5}As$ quantum dot in the surrounding GaAs, with a uniform (on average) composition profile, rather than accounting for the effects of spatial changes (nonuniform profile or ordering) in the overall composition [47,76–80]. We consider 300 random samples (lower part of Fig. 1), i.e., 300 different random realizations of the same alloyed lens-shaped quantum dot, with nominally the same average composition yet a different atomic arrangement on a microscopic scale.

III. RESULTS

To study the effects of alloy randomness, we focus on a uniform composition profile, rather than on the effects of spatial changes in the overall composition [78–80]. To model random alloy fluctuations, for each cation site a random number (uniformly distributed within a 0–1 range) is generated, and based on that a Ga atom is replaced with In with 0.5 probability. This approach will thus generate microscopic configurations that differ significantly in the atomic arrangement, while maintaining (on average) 50% gallium content. A more careful inspection reveals, however, that such a procedure may in fact result in random realizations that differ from average composition within an approximately ±1% range, as shown in Fig. 2(a). Therefore, a generated ensemble of quantum dots is subjected to (a) randomness due to a different atomic arrangement corresponding to the same composition, plus (b) small ($\pm \sim 1\%$) fluctuations of average composition. As shown in Fig. 2(b) the ground-state excitonic energy of the considered ensemble of quantum dots is altered by both effects. Changes in average composition (x axis in Fig. 2) correspond to a change of excitonic energy by approximately 8 meV per 1% of gallium content, consistent with the 10 meV estimate that can be obtained from the virtual crystal approximation (VCA) with bulk InGaAs parameters taken from Ref. [81]. However, changes on the vertical axis, which are also on a scale of several meV, are related purely to alloy randomness, which is going beyond the VCA. Importantly, whatever the cause, the exciton ground-state energy varies within relatively small ranges, namely less than 1.3% from an average of approximately 1257.6 meV. Therefore, since the average gallium content varies by at most 2%, one can speculate that substantial variations of the BES and the DES (as discussed in the following), which go far beyond the 2% range, are not related to changes in the average compositions, but they are due to (alloy) randomness. In other words, fluctuation of the average composition should contribute to at most 2% changes in spectra, whereas larger spectral changes are due to different microscopic atomic arrangements (random realizations) corresponding to the same (fixed) average composition.

In a standard treatment, the excitonic fine structure is typically [8,82] addressed by starting from idealized single-particle states, with electron spin states $|\pm\frac{1}{2}\rangle$ and the hole ground states of heavy-hole character associated with the projection of the total hole angular momentum: $|\pm\frac{3}{2}\rangle$. It is important to reemphasize that $|\pm\frac{1}{2}\rangle$ are not exactly equal to $e_\uparrow/e_\downarrow$ tight-binding eigenstates, which are not eigenfunctions of spin, but they are labeled with a pseudospin index instead. The same applies to the $h_\Uparrow/h_\Downarrow$ hole states as well. Nevertheless, $|\pm\frac{1}{2}\rangle$, $|\pm\frac{3}{2}\rangle$ states are of vital importance for defining effective Hamiltonians [8,83]. To this end, the excitonic basis of four states in such approaches is thus constructed from the above-mentioned idealized single-particle states, and it is characterized by their angular momentum projections,

$$|\pm 1\rangle = \left|\pm\frac{3}{2}, \mp\frac{1}{2}\right\rangle, \ |\pm 2\rangle = \left|\pm\frac{3}{2}, \pm\frac{1}{2}\right\rangle, \tag{5}$$

where the first value in the ket corresponds to the hole, and the second one corresponds to the electron. Matrix elements of the optical transition are given as [82] $M_{\pm\frac{3}{2},\mp\frac{1}{2}} \equiv M_{\pm 1} = M(e_x \mp ie_y)$, $M_{\pm 2} = 0$, where e_x, e_y are in-plane components of the **e** polarization vector, and M is independent of the light polarization. Therefore, $|\pm 1\rangle$ are optically active, whereas $|\pm 2\rangle$ are optically inactive states.

The electron-hole exchange Hamiltonian is expanded in the basis of these states, and in the order $|1\rangle, |-1\rangle, |2\rangle, |-2\rangle$ it can be written as [8]

$$\mathbf{H}_{\text{exch}} = \frac{1}{2}\begin{bmatrix} \delta_0 & \delta_1 & 0 & 0 \\ \delta_1 & \delta_0 & 0 & 0 \\ 0 & 0 & -\delta_0 & \delta_2 \\ 0 & 0 & \delta_2 & -\delta_0 \end{bmatrix}, \tag{6}$$

where δ_0 describes the dark-bright exciton splitting ("isotropic electron-hole exchange interaction"), δ_1 is responsible for the bright doublet splitting, and since it is related to distortions from idealized symmetry it is often called "anisotropic electron-hole exchange interaction," and finally δ_2 is responsible for the dark exciton splitting. For C_{3v} and D_{2d}, high-symmetry quantum dots $\delta_1 = 0$, i.e., bright exciton splitting, vanishes [19]. For C_{3v} systems, additionally $\delta_2 = 0$. Nonetheless, for realistic alloyed C_1 quantum dots, $\delta_1 \neq 0$ and $\delta_2 \neq 0$, and $\delta_1 \gg \delta_2$. Similar properties are shared by C_{2v}

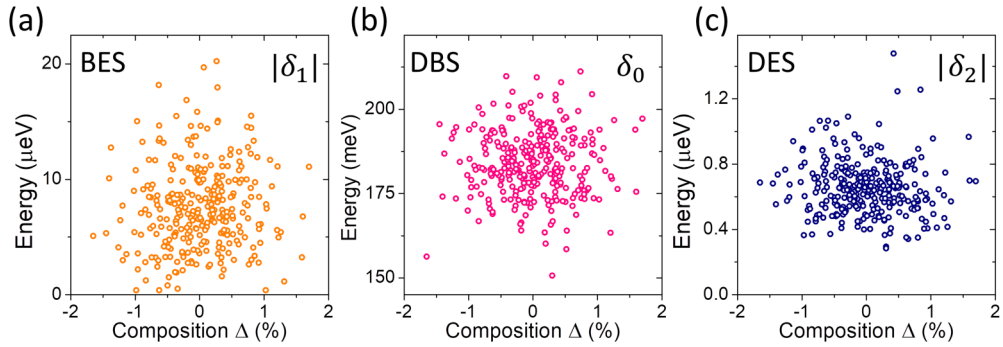

FIG. 3. Bright exciton splitting (a), dark-bright splitting (b), and dark exciton splitting (c) as a function of the difference from average composition (x axis), and alloy randomness (distribution of values along y axis). See the text for more details.

quantum dots, hence C_{2v} systems are often treated as good approximations to real system, although such approximations often fail [84,85], as also discussed in this work.

Since the off-diagonal block consists of zeros, there is no coupling between bright and dark manifolds, and they can be treated separately, with bright exciton states given as symmetric/antisymmetric combinations of basis states,

$$|\mathrm{BE1}\rangle = (|1\rangle - |{-1}\rangle)/\sqrt{2}, \tag{7}$$

$$|\mathrm{BE2}\rangle = (|1\rangle + |{-1}\rangle)/\sqrt{2}, \tag{8}$$

with analogous formulas for the dark exciton. Corresponding eigenenergies are given as

$$E_{\mathrm{BE1}} = (\delta_0 - \delta_1)/2, \tag{9}$$

$$E_{\mathrm{BE2}} = (\delta_0 + \delta_1)/2. \tag{10}$$

For the sake of comparison, atomistic results (calculated in a basis of 144 CI configurations) can be "recast" to the spectra of Eq. (6). For the nonalloyed, lens-shaped system of C_{2v} symmetry, we found from atomistic simulations that $\delta_1 > 0$, thus in such a case antisymmetric $|\mathrm{BE1}\rangle$ would be the lower-energy bright excitonic state. Moreover, $|\mathrm{BE1}\rangle$ is linearly polarized along the $[1\bar{1}0]$ direction, and $|\mathrm{BE2}\rangle$ is linearly polarized along [110]. Notably, there is no z-polarized emission allowed. For an alloyed system, polarization properties are more complicated, and they will be discussed in the following part of the paper.

The bright and dark exciton splittings calculated atomistically correspond to $|\delta_1|$, $|\delta_2|$ of the simple model, respectively, which are shown in Fig. 3. Excitonic fine structure does not show any clear trend with respect to average composition fluctuations, yet it strongly varies due to alloy randomness [21,86]. Bright exciton splitting [Fig. 3(a)] varies from zero to over 20 μeV, with an average value of 7.6 μeV and a standard deviation of 3.6 μeV. The dark-bright splitting [Fig. 3(b)] has an average value of 184 μeV, whereas the dark exciton splitting [Fig. 3(c)] varies from 0.28 to 1.48 μeV, with a mean value of 0.66 μeV and a standard deviation equal to 0.16 μeV. Again, albeit we considered the cylindrical quantum dot shape [85], both BES and DES are in good agreement with experimental values, although DES results are generally smaller than those observed in the experiment [9]. Nevertheless, we note that this range of DE energy level splittings corresponds to the precession periods [1] of a coherent superposition of DE eigenstates varying from 2.8 to 14.5 ns (with an average of 6.3 ns), thus again overlapping with typical experimental values [9,87].

To further analyze the polarization properties of bright excitons, while still assuming no dark-bright exciton coupling, one can use the Hamiltonian for the bright manifold only, derived based on group-theoretical [41] arguments:

$$\mathbf{H} = \begin{bmatrix} E+\delta & \kappa \\ \kappa & E-\delta \end{bmatrix}, \tag{11}$$

where E is the reference excitonic energy, δ (with no subscript) is responsible for the bright exciton splitting in the C_{2v} case due to lattice (and shape) anisotropy, whereas κ determines the fraction of the BES related to the contribution due to the lowering of symmetry caused by alloying. Moreover, κ is responsible for the coupling between the two bright states, leading to the rotation [41] of the emission lines from the perfect crystal directions. This polarization angle θ is given as $\tan(\theta) = \frac{\delta}{\kappa} \pm \sqrt{1 + (\delta/\kappa)^2}$, with the overall bright exciton splitting given as $\delta_1 = 2\sqrt{\delta^2 + \kappa^2}$, and conversely

$$\kappa = -\frac{\delta_1}{2}\sin(2\theta),\ \ \delta = \frac{\delta_1}{2}\cos(2\theta) \tag{12}$$

with bright eigenstates given as

$$|\mathrm{BE}_1\rangle = -|\sin(\theta)\rangle + |\cos(\theta)\rangle, \tag{13}$$

$$|\mathrm{BE}_2\rangle = |\cos(\theta)\rangle + |\sin(\theta)\rangle. \tag{14}$$

Model Eq. (11) allows us to decompose the bright exciton splitting into two contributions, due to anisotropy (δ) and alloying (κ), respectively, which are shown in Fig. 4. The κ mean value, $\langle\kappa\rangle$, is close to zero, indicating a lack of any directional character of alloying, whereas δ has a mean value of -2.32 μeV, which is due to lattice anisotropy. This result is in vivid contrast to atomistic pseudopotential calculations [86], where $\langle\delta\rangle$ is different from zero only for elongated quantum dots. This result is, however, consistent with the systematic difference between empirical tight-binding and empirical pseudopotential approaches for C_{2v} systems [49], as well BES reported experimentally [47].

κ and δ have standard deviations σ of 2.66 and 2.30 μeV, respectively. Since both κ and δ are apparently independent,

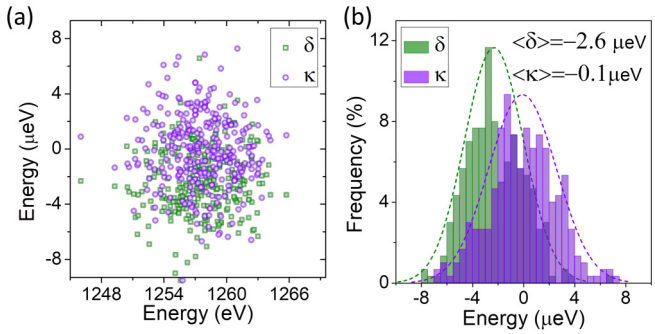

FIG. 4. (a) δ and κ contributions to the BES as a function of excitonic ground-state energy. Histogram (b) of δ and κ with mean κ (contribution due to alloying) value close to zero, mean δ (contribution due to lattice anisotropy) different from zero. Note that when graphs overlap, a different color is used. See the text for details.

and have a distribution that can be quite well described by the normal distribution [Fig. 4(b)], with $\sigma = \sigma_\delta \approx \sigma_\kappa = 2.6\ \mu$eV, and $\langle\delta\rangle$ not exceeding σ, one can expect that $\delta_1 = 2\sqrt{\delta^2 + \kappa^2}$ will follow the Rayleigh distribution [88,89] (i.e., essentially a χ distribution with two degrees of freedom):

$$P(\delta_1) = \frac{\delta_1}{4\sigma^2} \exp\left(-\frac{\delta_1^2}{8\sigma^2}\right), \tag{15}$$

where the denominator is multiplied by a factor of 4 (with respect to the original Rayleigh distribution), due to 2 occurring in the definition of δ_1, i.e., $\delta_1 = 2\sqrt{\delta^2 + \kappa^2}$. Figure 5(a) shows a histogram of BES values with Eq. (15) plotted with a dotted black line revealing a rather good fit, despite not strictly fulfilling the assumption of $\langle\delta\rangle = 0$, and with $\sigma = 2.66$ not taken as a fitting parameter. Thus, as a result of δ_1 having a two-component character, its distribution varies from the normal distribution, but it resembles χ with $k = 2$. Rayleigh distribution is derived for the system of two dimensions, however the mathematical form of the Rayleigh distribution is identical to the Wigner surmise for the one-dimensional energy levels problem [86,89],

$$P(s) = \frac{\pi}{2} s \exp\left(-\frac{\pi}{4} s^2\right), \tag{16}$$

with $s = \delta_1/\langle\delta_1\rangle$, and where $\langle\delta_1\rangle = 7.60\ \mu$eV was calculated as an average BES of all 300 samples. The plot of Eq. (16) is

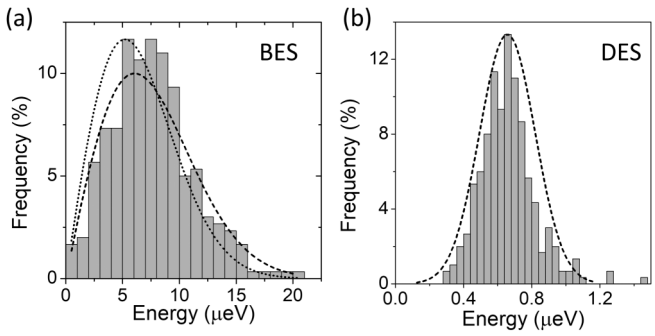

FIG. 5. Histogram of (a) the bright exciton splitting [with the dotted (dashed) line corresponding to Rayleigh (Wigner) distributions], and (b) dark exciton splitting (the dashed line is a fit to a normal distribution).

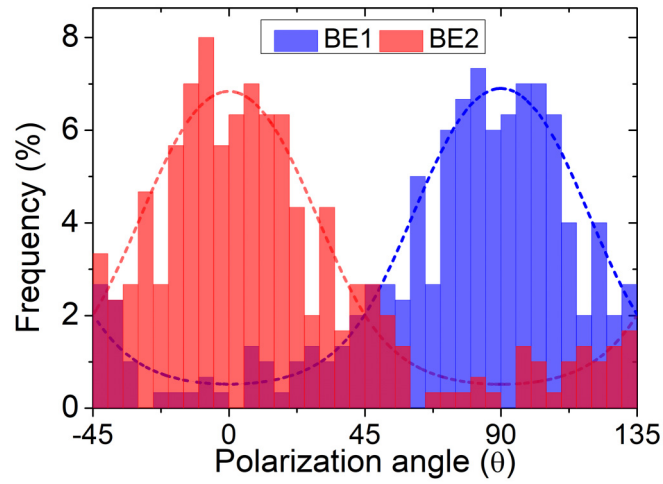

FIG. 6. Histograms of polarization angle for lower (BE1) and higher (BE2) energy bright exciton states with maxima corresponding to [110] and [1$\underline{1}$0] crystal axes (0° and 90°, respectively). The dashed lines are calculated using the approach from Ref. [86]. Note that when graphs overlap, a different color is used. See the text for details.

also shown in Fig. 5(a) with a dashed line, compared with the histogram of BES values. We note that Eqs. (15) and (16) have identical mathematical forms, whereas the difference between plots in Fig. 5(a) is related to the difference in parameters describing "variances" of both distributions (i.e., $\langle\delta_1\rangle \neq \sqrt{2\pi}\sigma$).

Since Eq. (16) corresponds to the standard level-spacing distribution of the Gaussian orthogonal ensemble in random matrix theory, Gong *et al.* [86] argue that this sort of statistical dependence reveals strong repulsion between excitonic levels, and the presence of multiplicative s in Eq. (16) reduces the probability of finding quantum dots with small BES. As a result of this sort of behavior, we find that over 50% of the samples have BES within 5–10 μeV, while only 3.4% of cases have BES larger than 15 μeV, and importantly only 1.7% of cases have BES smaller than 1 μeV. BES smaller than the linewidth (of approximately 1 μeV) is important in the context of entanglement generation. Results presented here may look counterintuitive, since cylindrical quantum dots seem to be good candidates for small BES values, yet they are consistent with earlier findings [86].

For comparison, Fig. 5(b) shows a histogram of the DES values revealing normal distribution with a mean of 0.657 and a standard deviation of 0.16 μeV. Thus, the DES is an order of magnitude smaller than the BES, however in systems studied here it is virtually impossible to find a quantum dot with a vanishing dark exciton splitting.

Finally, we note that mixing with higher shells increases both BES and DES. If only the s-shell were included in the atomistic calculation (corresponding to 4×4 CI Hamiltonian), the mean BES value would be 4 μeV, and the DES mean value would be 0.53 μeV, with no substantial qualitative difference in histograms. For comparison, atomistic results obtained for the s-shell only are presented in Appendix A.

Statistical analysis performed for κ and δ can be performed for the bright exciton polarization angle as well, with results shown in Fig. 6, where the histogram obtained from the

current atomistic calculation is compared with a statistical model (dashed line) from the supplementary information of Ref. [86]. The lower-energy bright exciton state (BE1) tends to be polarized along the $[1\bar{1}0]$ direction (rotated by 90° from [110]), whereas the higher-energy one (BE2) prefers polarization along the [110] direction. Therefore, despite substantial alloying (and overall cylindrical shape), the polarization angle dependence has well-defined maxima corresponding to the vicinity of crystal axis. This is again in stark contrast to empirical pseudopotential results [86] that predict pronounced polarization angle distribution maxima only for elongated dots. This difference can be traced back to the δ distribution as shown earlier (Fig. 4): in the atomistic tight-binding calculation, $\langle\delta\rangle \neq 0$, contrary to the empirical pseudopotential method. This is consistent with the latter systematically underestimating the lattice BES contribution, the origin of which remains to a large degree unexplored [47], with the claim from Ref. [47] that "the variations in shape, size, or composition, we can assume theoretically, are not able to bring theory and experiment in agreement," and suggesting that ordering effects as the source of the disagreement.

The model of Eq. (11) assumes the angle between bright excitons to be exactly equal to 90°. To go beyond that, and further study polarization properties, the exchange Hamiltonian can explicitly account for phases of electron-hole exchange interaction [82,90],

$$\mathbf{H}_{\text{exch}} = \frac{1}{2}\begin{bmatrix} \delta_0 & \delta_1 e^{-2i\theta_1} & 0 & 0 \\ \delta_1 e^{2i\theta_1} & \delta_0 & 0 & 0 \\ 0 & 0 & -\delta_0 & \delta_2 e^{-2i\theta_2} \\ 0 & 0 & \delta_2 e^{2i\theta_2} & -\delta_0 \end{bmatrix}, \tag{17}$$

where θ_1 describes the rotation of the polarization axis (around the growth axis z) by the angle θ_1 with respect to the fixed axes, usually taken as the crystal axis [110]. The eigenstates have the following form:

$$|\text{BE}_{1,2}\rangle = \big(|1\rangle \pm e^{-2i\theta_1}|{-1}\rangle\big)/\sqrt{2}, \tag{18}$$

$$|\text{DE}_{1,2}\rangle = \big(|2\rangle \pm e^{-2i\theta_2}|{-2}\rangle\big)/\sqrt{2}. \tag{19}$$

By comparing with atomistic calculations, we find that the nonalloyed C_{2v} system $2\theta_1 = \pi$ and $2\theta_2 = \frac{3}{2}\pi$, indicating a $\pi/2$ phase difference between dark and bright manifolds.

While Eq. (17) enables us to understand the rotation of the quantum dot principal axes with respect to the crystal axes, it still by definition predicts exactly vanishing polarization anisotropy [90], i.e., $C = (I_{\max} - I_{\min})/(I_{\max} + I_{\min}) = (I_{\text{BE2}} - I_{\text{BE1}})/(I_{\text{BE2}} + I_{\text{BE1}}) = 0$, since the magnitudes of the emission intensities of both bright excitons are exactly equal.

To go beyond this picture, and to allow for better agreement with the experiment, one can account for valence-band mixing, which occurs in realistic quantum dots, due to shape asymmetry and lattice anisotropy, leading to an admixture of light-hole components,

$$|\pm\widetilde{1}\rangle = \sqrt{1-\beta^2}\left|\pm\frac{3}{2}, \mp\frac{1}{2}\right\rangle + \beta e^{\pm 2i\psi}\left|\mp\frac{1}{2}, \mp\frac{1}{2}\right\rangle, \tag{20}$$

where β and ψ are the amplitude and the phase of mixing with a light-hole exciton $|\mp\frac{1}{2}, \mp\frac{1}{2}\rangle$, and a tilde symbol was used to distinguish from the basis with no band-mixing included. A similar formula is used for dark states,

$$|\pm\widetilde{2}\rangle = \sqrt{1-\beta^2}\left|\pm\frac{3}{2}, \pm\frac{1}{2}\right\rangle + \beta e^{\pm 2i\psi}\left|\mp\frac{1}{2}, \pm\frac{1}{2}\right\rangle. \tag{21}$$

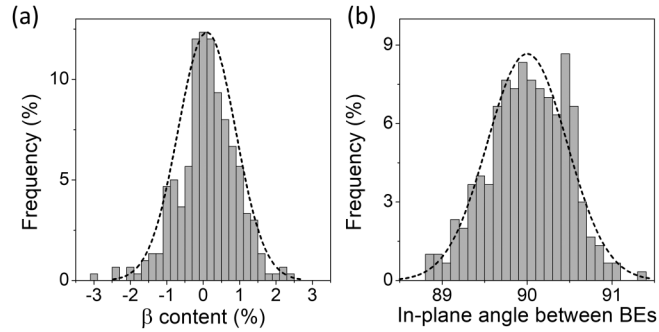

FIG. 7. Histogram of (a) β light-hole content for an ensemble of alloyed quantum dots, and (b) in-plane angle difference between lower (BE1) and higher (BE2) energy bright exciton states. The dashed lines are plotted assuming normal distribution. Despite alloying, β content remains rather small, with the angle between bright excitons close to 90°. See the text for more details.

The exchange Hamiltonian expressed in the basis $|\pm\widetilde{1}\rangle$, $|\pm\widetilde{2}\rangle$ maintains the block-diagonal structure of Eq. (6) and its eigenstates, but with tilded states replacing $|\pm1\rangle$, $|\pm2\rangle$. β is responsible for polarization anisotropy [90,91],

$$C(\beta) = \frac{2\beta\sqrt{3(1-\beta^2)}}{3-2\beta^2}. \tag{22}$$

Polarization anisotropy is naturally present in atomistic calculation, and for a C_{2v} system it reaches 2.9% with emission intensity for $|\text{BE2}\rangle$ along [110] larger than for $|\text{BE1}\rangle$ along the $[1\bar{1}0]$ direction. Recasting atomistic C_{2v} results on a valence-band-mixed 4×4 Hamiltonian give a β value of 2.5%. Moreover, for the C_{2v} quantum dot mixing phase, $\psi = 0$, and emission lines remain orthogonal [83,90].

For alloyed systems, both β and ψ determine an angle between excitonic lines, which in principle can be different from 90°. Figure 7(a) shows a histogram of β values for alloyed systems studied in this paper, which appears to be normally distributed around zero light-hole content, with both positive and negative light-hole mixing amplitudes possible, and most of the cases corresponding to $|\beta| < 1\%$. Moreover, as shown in Fig. 7(b), valence-band mixing allows for the angle between polarizations of bright excitonic lines to be different from the exact 90°, however for the vast majority of cases this difference does not exceed 1°, rendering Eq. (11) a valid approximation for the considered ensemble of quantum dots.

Valence-band mixing, expressed via the nonzero β content, has its effect on the dark manifold as well, since $|\pm\widetilde{2}\rangle = \sqrt{1-\beta^2}|\pm\frac{3}{2}, \pm\frac{1}{2}\rangle + \beta e^{\pm 2i\psi}|\mp\frac{1}{2}, \pm\frac{1}{2}\rangle$, and since matrix elements of the optical transition [82,83] for the light-hole component are given as $M_{\mp\frac{1}{2},\pm\frac{1}{2}} \propto e_z$, dark excitons $|\pm\widetilde{2}\rangle$ get optical activity due to hole band mixing, which is proportional to β, i.e., $|M_{\pm\widetilde{2}}|^2 \propto \beta^2[1 \mp \cos 2(\theta_2 - 2\psi)]$. For the C_{2v} system, $\psi = 0$ [83], and since from atomistic calculation $2\theta_2 = \frac{3}{2}\pi$ and $\delta_2 > 0$, only one of the dark exciton states

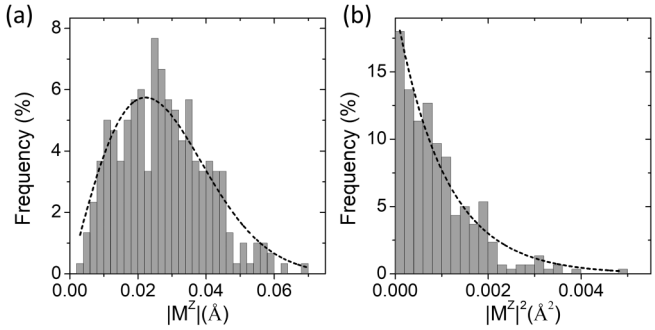

FIG. 8. Histogram of (a) modules of out-of-plane single-particle optical dipole moment $|M^z| = |M^z_{e\uparrow,h\Uparrow}| = |M^z_{e\downarrow,h\Downarrow}|$, and (b) its squared moduli. The dashed lines are calculated assuming probability distributions discussed in the text, suggesting the two-component character of the optical dipole moment.

(higher energy, DE2) is optically active, which allows the DE emission perpendicular to the growth direction to be detected, and the other (lower energy, DE1) remains fully dark, in agreement with experimental findings [92].

Moreover, group-theoretical arguments indicate that the optical dipole moment (matrix elements of the optical transition) for the dark exciton can be nonzero even for a pure heavy-hole exciton, i.e., $|M_{\mathrm{DE2}}|^2 \propto e_z$ even if $\beta = 0$, whereas DE1 remains optically inactive, i.e., $|M_{\mathrm{DE1}}|^2 = 0$. Thus, the single-particle dipole matrix element for z-polarized light, calculated on the basis of tight-binding states, is $|M^z| = |M^z_{e\uparrow,h\Uparrow}| = |M^z_{e\downarrow,h\Downarrow}| \propto |\beta M_{\mathrm{LH}} + M_{\mathrm{HH}}|$, and therefore it could be interpreted as having light- and heavy-hole components. It is not straightforward to perform such decomposition for atomistically obtained states. We have thus tried an approximate attempt by applying a vertical electric field, aiming to use the field to reduce the polarization anisotropy of the bright exciton to zero, for which case, based on Eq. (22), one can assume $\beta \sim 0$. In such a situation, $|M^z|$ should only have the heavy-hole component, which could be estimated in this way. By performing such an analysis for the C_{2v} system, we found $M_{\mathrm{LH}} = -0.042$ Å and $M_{\mathrm{HH}} = 0.051$ Å. Therefore, both contributions can have comparable magnitudes and opposite signs, thus they can partially cancel each other. Despite its approximated character, we have performed a similar study for five alloyed systems as well, and we came to similar conclusions. To further analyze $|M^z|$ distributions in the considered ensemble of an alloyed system, we show its histogram in Fig. 8(a), and then the $|M|^2$ histogram in Fig. 8(b). The $|M^z|$ distribution can be well fit to the χ distribution with two degrees ($k = 2$) of freedom, which is mathematically equivalent to the Rayleigh distribution/Wigner surmise discussed earlier [i.e., $\sim x \exp(-\frac{\pi}{4}x^2)$], with $x = |M^z|/\langle|M^z|\rangle$ shown as a dotted line in Fig. 8(a). Therefore, it is expected that $|M^z|^2$ would be well described by the χ^2 distribution, again with two degrees of freedom, corresponding to the exponential distribution $\sim\exp(-x)$. In other words, Fig. 8 indirectly supports a two- (light- and heavy-hole) component character of the single-particle dipole moment $|M^z|$. Aside from speculations regarding heavy- and light-hole contributions, since M^z is a complex number, Rayleigh distribution is expected [89] when real and imaginary components are independently and identically (Gaussian) distributed (with equal variance and zero mean). In such a case, the absolute value of the complex number is Rayleigh-distributed, as apparently shown in Fig. 8, thus supporting the two-component character of M_z irrespective of its origin.

Finally, after an analysis of single-particle transition matrix elements, we can study many-body dark exciton optical spectra, shown for z-polarization in Fig. 9. Should the single-particle optical dipole moments be artificially neglected, i.e., $|M_{e\uparrow,h\Uparrow}| = |M_{e\downarrow,h\Downarrow}| = 0$, both dark excitons would not reveal any significant optical activity. The residual weak activity [Fig. 9(a)] may be attributed to the dark-bright mixing term (due to exchange interaction) present in the atomistic calculation that will be discussed in the following part of the paper. In the case of z-polarized dark exciton emission, exchange mixing apparently does not play any significant role. However, the inclusion of a nonzero optical matrix element leads to a substantial increase in z-polarized emission as seen in Fig. 9(b). This increase is particularly important for the higher-energy DE2 states, for which it can reach over 0.006 Å^2, i.e., approximately 1/6000 of bright exciton emission merely due to alloying. DE1 states gain some optical activity as well, which is, however, much smaller, and what seems to be a property "inherited" from the C_{2v} system since both the amplitude and phase of valence-band mixing, i.e., β (and apparently ψ), remain rather small in the alloyed system. Notably, further extension of the CI basis by inclusion of higher shells [Fig. 9(c)] does not seem to affect dark exciton optical spectra, indicating the dominant contribution is from the optical dipole moment and not due to configuration mixing.

In a phenomenological treatment, several authors further extend the valence-band mixing approach by accounting for a mixing term between heavy- and light-hole states with parallel spins:

$$\begin{aligned}|\pm\tilde{\tilde{1}}\rangle =& \sqrt{1-\beta^2-\gamma^2}\left|\pm\frac{3}{2},\mp\frac{1}{2}\right\rangle \\ &+ \beta e^{\pm 2i\psi}\left|\mp\frac{1}{2},\mp\frac{1}{2}\right\rangle + \gamma e^{\pm 2i\xi}\left|\pm\frac{1}{2},\mp\frac{1}{2}\right\rangle \end{aligned} \tag{23}$$

with a similar formula for $|\pm\tilde{\tilde{2}}\rangle$ dark states, and where γ and ξ are the amplitude and the phase of mixing, and the double tilde symbol is used to distinguish from previously considered cases. This approach has been used to study the z-polarized emission of bright excitons [90], with the γ parameter being far more difficult to extract from the experiment (or atomistic calculations) than β, and thus we will not aim for doing that. However, it was also shown recently [44] that mixing the γ term induces off-diagonal Hamiltonian matrix elements (exchange integrals) responsible for the dark-bright exciton mixing:

$$\begin{aligned}\mathbf{H}_{\mathrm{exch}} &= \frac{1}{2}\begin{bmatrix} \delta_0 & \delta_1 e^{-2i\theta_1} & \delta_{11} & \delta_{12} \\ \delta_1 e^{2i\theta_1} & \delta_0 & -\delta_{12} & -\delta_{11} \\ \delta^*_{11} & -\delta^*_{12} & -\delta_0 & \delta_2 e^{-2i\theta_2} \\ \delta^*_{12} & -\delta^*_{11} & \delta_2 e^{2i\theta_2} & -\delta_0 \end{bmatrix} \\ &= \frac{1}{2}\begin{bmatrix} \mathbf{H}_{\mathrm{BB}} & \mathbf{H}_{\mathrm{BD}} \\ \mathbf{H}_{\mathrm{DB}} & \mathbf{H}_{\mathrm{DD}} \end{bmatrix}, \end{aligned} \tag{24}$$

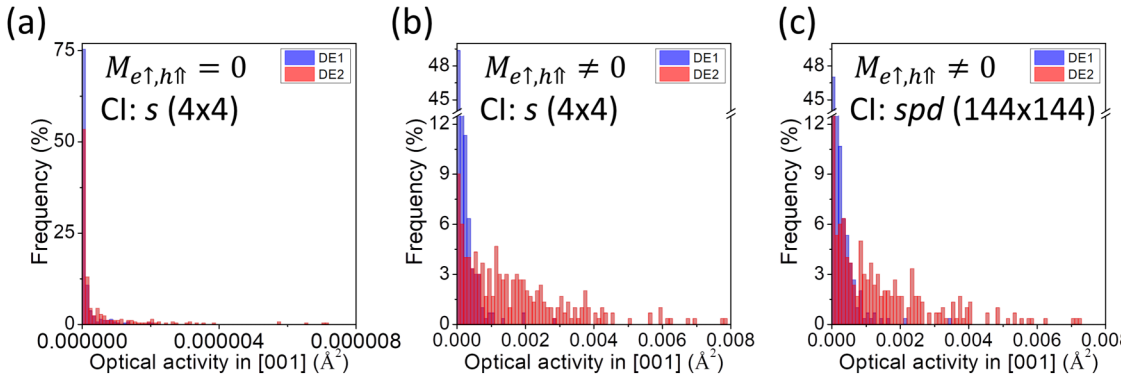

FIG. 9. Histogram of z-polarized (out-of-plane) optical spectra for lower (DE1) and higher (DE2) dark exciton states for cases with (a) optical dipole moment artificially set to zero ($M_{e\uparrow,h\Uparrow} = 0$ and $M_{e\downarrow,h\Downarrow} = 0$), (b) optical dipole moment included in the calculation, and (c) calculation performed in a basis including s, p, and d shells of 144 excitonic configurations. The z-polarized dark exciton activity thus stems from nonzero optical dipole moment (due to valence-band mixing), whereas the exchange mixing plays a negligible role, and higher shells play a rather small role as well. Note that when graphs overlap, a different color is used. See the text for more details.

where $\mathbf{H}_{\mathrm{DB}}$ denotes dark-bright coupling for brevity, whereas δ_{11} and δ_{12} are responsible for mixing of bright and dark configuration states differing by the electron and the hole spin state, respectively, i.e., δ_{11} mixes $|\tilde{\tilde{1}}\rangle$ with $|\tilde{\tilde{2}}\rangle$, and δ_{12} mixes $|-\tilde{\tilde{1}}\rangle$ with $|-\tilde{\tilde{2}}\rangle$. With the exception of phase factors, an identical Hamiltonian can also be derived in a phenomenological manner by assuming the rotation of quantum-dot axes (angular-momentum quantization axes) from the ideal crystal axes [43]. A virtually identical Hamiltonian is also derived from atomistic calculations for C_s quantum dots, where low shape symmetry induces mixing between bright and dark states [10].

Interestingly, we also found an identical structure of the (lowest four states) Hamiltonian from atomistic calculations for the currently studied alloyed quantum dot despite their cylindrical symmetry and the lack of faceting. Therefore, not only can shape deformation induce bright-dark exciton exchange coupling, but breaking the symmetry on the scale of local atomic arrangement can lead to the same effect. Moreover, despite the overall C_1 symmetry, the dark-bright coupling block derived from atomistic calculation in a basis of tight-binding states $|e_\uparrow, h_\Uparrow\rangle, |e_\downarrow, h_\Downarrow\rangle|$ is given as

$$\mathbf{H}_{\mathrm{DB}} = \begin{bmatrix} \delta_{11} & \delta_{12} \\ -\delta_{12}^* & -\delta_{11}^* \end{bmatrix}, \tag{25}$$

where the only difference from the phenomenological Hamiltonian Eq. (24) (expressed in a double-tilde basis) is related to complex conjugations in the second row.

IV. DARK EXCITON IN-PLANE OPTICAL ACTIVITY

To further study the role of dark-bright exciton mixing, in Fig. 10(a) we show histograms of δ_{11} and δ_{12}. The absolute value of δ_{12} can be quite well fit to $x\exp(-x^2)$, which is again equivalent to the χ distribution with $k = 2$, suggesting a two-component character of δ_{12} integral. This is consistent with Ref. [43], where it was interpreted in terms of two effective tilt angles (one related to the electron, and the second to the hole) leading to the dark-bright mixing. This is also coherent with the approach of Ref. [44], where δ_{12} is induced by the presence of both β and γ mixing terms. In the treatment employed in Ref. [44], δ_{11} depends on γ only. One can thus expect its statistical distribution to differ from that found for δ_{12}, and in fact this is visible in Fig. 10(a), where one can fit δ_{11} to $x\exp(-x)$, resembling γ distribution with $k = 1$. Whereas this sort of analysis is speculative, δ_{11} undoubtedly varies from 0 to 2.7 μeV with a mean (average) of 0.5 μeV, and δ_{12} varies from 0 to 3.05 μeV with a mean of 1 μeV. Therefore, δ_{11} and δ_{12} have magnitudes comparable to δ_1, the dark exciton splitting, and thus *a priori* cannot be neglected when considering the excitonic fine structure of an alloyed system. Moreover, both BES and DES will be renormalized by the presence of dark-bright coupling [43,44]. However, since the correction is equal to $\delta_{11}\delta_{12}/\delta_0$, the effect of dark-bright mixing on both BES and DES is negligible for the system considered in this work, as we have $\delta_0 \gg \delta_{11,12}$.

For C_{2v} quantum dots, by symmetry, both dark excitons are strictly optically inactive when considering the in-plane polarization. For a C_1 quantum dot, however, there are two channels through which dark excitons can gain in-plane optical activity (see Appendix C for more details). One of them is related to the dark-bright exchange interaction, which was already mentioned above, and in which the dark exciton can gain optical activity from the admixture of bright configurations. The second channel is related to a nonvanishing dipole moment

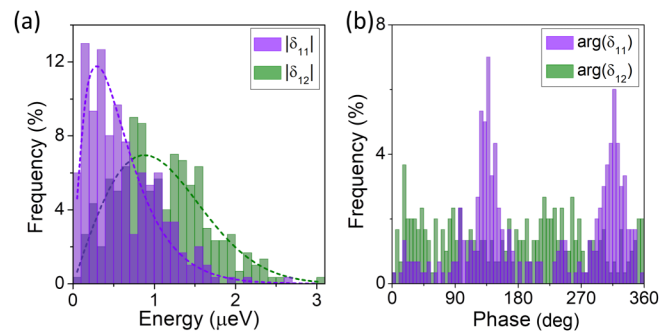

FIG. 10. Histogram of (a) moduli (absolute values) of δ_{11} and δ_{12} dark-bright mixing integrals, and (b) their arguments (phases). Note that when graphs overlap, a different color is used.

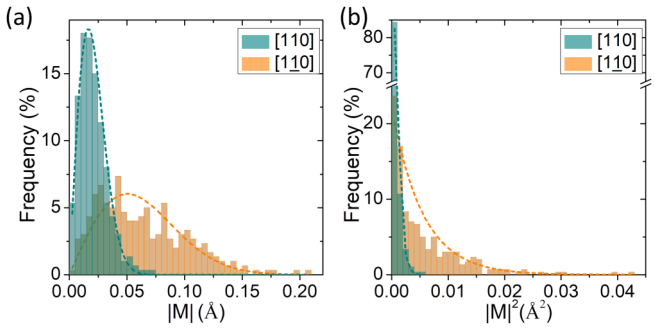

FIG. 11. Histograms of (a) moduli of in-plane single-particle optical dipole moments for light polarized in [110] and [1$\bar{1}$0] directions, i.e., $|M^{[110]}_{e\uparrow,h\Uparrow}|$ and $|M^{[1\bar{1}0]}_{e\downarrow,h\Downarrow}|$, and (b) their squared moduli. The dashed lines are calculated assuming probability distributions discussed in the text. Note that when graphs overlap, a different color is used.

for in-plane (x, y) polarized light $M^{x,y}_{e\uparrow,h\Uparrow} \neq 0$ and $M^{x,y}_{e\downarrow,h\Downarrow} \neq 0$, similarly to the M^z dipole moment discussed earlier.

Figure 11 shows histograms of in-plane dipole moment matrix elements along two experimentally relevant crystal axes, [110] and [1$\bar{1}$0]. Importantly, $|M|^{[1\bar{1}0]}$ has a substantially larger magnitude than $|M|^{[110]}$, thus despite alloying and the cylindrical shape of quantum dots in the ensemble, the lattice anisotropy still plays an important role with the average $\langle|M|^{[1\bar{1}0]}\rangle = 0.063$ Å three times larger than $\langle|M|^{[110]}\rangle = 0.021$ Å.

We note as well that $|M|^{[1\bar{1}0]}$ is larger than the one for the z-polarized case, i.e., $\langle|M|^{[001]} \equiv \langle|M|^z\rangle$ (shown earlier in Fig. 8). This may be understood since quantum-dot lateral dimensions are substantially larger than the in-growth (z) directions. However, similarly to $|M^z|$, $|M|^{[1\bar{1}0]}$ (as well as $|M|^{[110]}$) can be very well approximated by χ distribution with $k = 2$, and with $|M|^2$ [Fig. 11(b)] showing a χ^2 dependence, with $k = 2$, i.e., the exponential distribution.

Since in-plane single-particle dipole moment matrix elements are nonzero, as are the dark-bright exchange mixing terms in the Hamiltonian, it is instructive to study how these terms individually affect many-body dark exciton optical spectra. To this end, in Fig. 12(a) we show the results with dark-bright mixing artificially neglected, and with the single-particle dipole moment being the only term inducing dark exciton in-plane optical activity. In this case, DE2 has much larger optical activity than DE1, similarly to previously considered out-of-plane emission. Alternatively, exchange mixing can be artificially neglected and optical dipole moments accounted for, as in Fig. 12(b). Such a situation produces very similar optical spectra to the first case, with DE2 having substantially larger optical activity than DE1, despite a different mechanism of luminescence.

Interestingly, when both terms are included [Fig. 12(c)], they appear to partially compensate each other, with the dark exciton optical activity on average an order of magnitude smaller compared to the (a) and (b) cases, thus comparable with the out-of-plane emission. A notable difference from z-polarized emission can, however, be observed, since both DE1 and DE2 have (on average) similar optical activity.

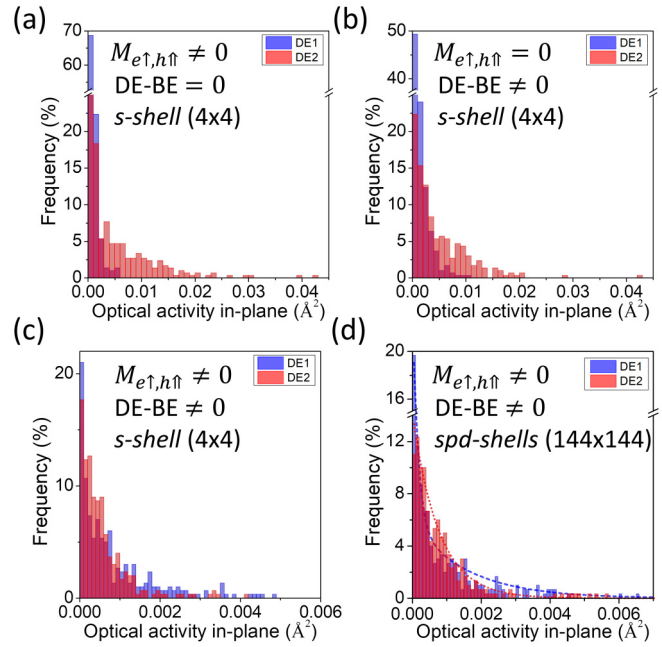

FIG. 12. Histogram of in-plane optical spectra (emission intensity) for lower (DE1) and higher (DE2) dark exciton states with (a) optical single-particle dipole moment included in the calculation, but exchange dark-bright mixing terms neglected ($\delta_{11} = \delta_{12} = 0$) in the Hamiltonian, (b) optical dipole moment artificially set to zero ($|M_{e\uparrow,h\Uparrow} = 0$ and $M_{e\downarrow,h\Downarrow} = 0$), but exchange mixing accounted for, (c) both contributions included, and (d) as in (c) but with calculation performed in a basis including s, p, and d shells of 144 excitonic configurations. Note the different scales, as well as the presence of breaks on vertical axes. Apparently, both nonzero optical dipole moments and exchange mixing play equally important roles, and none of these contributions can be neglected, as it would result in an overestimation of the optical activity. Note that when graphs overlap, a different color is used. See the text for more details.

Therefore, reduction of symmetry due to alloying must be accounted for in both the transition dipole moment and exchange matrix elements on an equal footing. Failing to do so leads to a serious overestimation of the dark exciton in-plane optical activity. This could be understood in the spirit of Ref. [43], where the reduction of symmetry is related to the rotation of quantum dot axes. This new quantization axis, or rotation of angular momenta, must be included simultaneously in the calculation of the single-particle dipole moment and two-body Coulomb and exchange integrals.

Moreover, we find that for C_1 alloyed quantum dots it is impossible to fit atomistic spectra to the effective 4×4 Hamiltonian [formally resembling Eq. (24)] with an idealized matrix element of the optical transition (i.e., vanishing in-plane optical dipole moments), and with δ_{11}, δ_{12} being the only factors responsible for the dark-exciton optical activity. Such a procedure was indeed possible for C_s systems [10], however for C_1, since both dipole moments and the Coulomb matrix are affected by alloying, one would need to include two additional fitting parameters in the Hamiltonian (δ_{21} and δ_{22} integrals) to further differentiate coupling of bright and dark states, which does not have a formal justification. Thus, we again conclude that the calculation of dipole moments and Coulomb

matrix elements in an alloyed system must be performed on an equal footing, unless some other factor (speculatively a large quantum dot shape deformation/anisotropy) dominates over alloying.

Further inclusion of higher shells beyond the 4×4 CI treatment does not change the overall picture [Fig. 12(d)] considerably. In this case, despite the complicated origin of dark exciton activity (dipole moments, exchange mixing, and CI), the frequency distribution of optical activity can be quite well fit with a single exponent for DE2 states, and with two exponents for DE1. Interestingly, optical activity larger than 0.002 Å^2 seems to be dominated by that coming from DE1 states. So for several samples, the combined effect of nonzero dipole moments and dark-bright mixing leads noticeably to more pronounced emission from the lower-energy dark exciton state, although this is a rather subtle effect. Such activity would be in agreement with experimental results [2], although here we do not aim at a comparison with a particular experiment. Due to alloy randomness, the dark exciton in-plane activity reaches 1/6000 of the bright exciton activity, with the average of 1/40 000, thus considerably smaller that that observed when a shape distortion [10] is the source of dark excitonic optical activity. Nevertheless, we can conclude that a mere reduction of overall symmetry due to alloy randomness is able to trigger non-negligible in-plane polarized optical activity of dark excitons in self-assembled InGaAs quantum dots.

Finally, it is worthwhile to conduct a similar analysis for the polarization angle of the dark exciton in-plane emission, as shown in Fig. 13. With either dark-bright exchange mixing artificially neglected [Fig. 13(a)] or dipole moments set to zero [Fig. 13(b)], the angle of polarization of both dark excitons tends to prefer 90° rotation from [110], i.e., polarization along the $[1\bar{1}0]$ direction. This is particularly pronounced for DE2 states. Therefore, with either contribution accounted for while the other is neglected, the in-plane spectra of dark excitons somewhat resemble the out-of-plane (z) polarized spectra with DE2 having dominant optical activity.

However, the situation is apparently different with both contributions simultaneously included, as shown in Fig. 13(c), where DE1 (in particular) and DE2 (to a lesser degree) preferable polarization is along [110] (polarization angle 0°). This is somewhat opposite to experimental observation, where the dominant emission is from the lower dark exciton state, following polarization from the lower-energy bright exciton state. However, caution must be exercised since experiments are unavoidably performed on nonideal, low shape symmetry QDs. Our atomistic results [10] for a quantum dot with a facet, and thus broken shape symmetry, indeed indicated a very good agreement with a particular experiment [2,9]. Thus, a deviation from the cylindrical base very likely must be included when one aims for a comparison with a particular experimentally grown system, and here we focus on the alloy randomness effect only.

Since both DE1 and DE2 appear to have their polarization preferably along the [110] direction, it is instructive to show the histogram of angles between polarizations of DE1 and DE2 states (for their in-plane emission) as shown in Fig. 14. Contrary to bright excitons [shown earlier in Fig. 5(b)], where the polarization directions strongly tend to be orthogonal (i.e., the angle between polarizations close to 90°), the dark exciton states tend to be polarized along the same direction, however due to alloy randomness virtually any angle between these two emission lines is possible. Again, accounting for shape elongation or faceting in a particular experimental realization together with alloy randomness could very likely change these statistics.

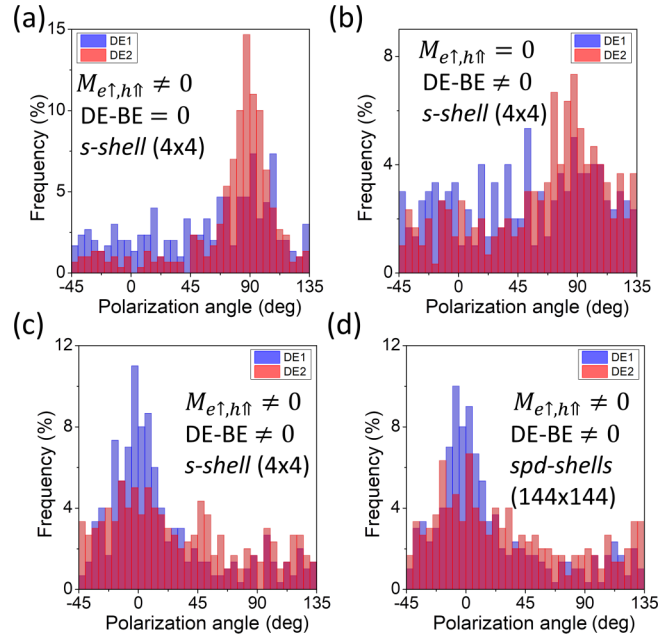

FIG. 13. Histogram of in-plane polarization angle for lower (DE1) and higher (DE2) dark exciton states with (a) optical single-particle dipole moment included in the calculation, but exchange dark-bright mixing terms neglected ($\delta_{11} = \delta_{12} = 0$) in the Hamiltonian, (b) optical dipole moment artificially set to zero ($|M_{e\uparrow,h\Uparrow} = 0$ and $M_{e\downarrow,h\Downarrow} = 0$), but exchange mixing accounted for, (c) both contributions included, and (d) as in (c) but with calculation performed in a basis including s, p, and d shells of 144 excitonic configurations. Again, both nonzero optical dipole moments and exchange mixing play equally important roles, and none of these contributions can be neglected. Note that when graphs overlap, a different color is used. See the text for more details.

Moreover, there is still little experimental data regarding dark exciton spectra, since measurements are usually performed on a single quantum-dot sample only. Our calculation indicates that for alloyed quantum dots, one can cherry-pick a sample with DE1 polarized along [110] or $[1\bar{1}0]$, with DE1 being the dominant line, or vice versa. Therefore, more experimental research on the subject is needed.

V. RADIATIVE LIFETIMES

In Sec. IV, we studied the dark exciton optical activity. For comparison, therefore, Fig. 15 shows a histogram of both bright exciton states' optical activities, which are apparently normally distributed around approximately 39.5 Å^2, corresponding to a mean optical dipole moment of 0.63 nm, with rather small variance corresponding to dipole moments from 0.6 to 0.66 nm, thus very close to typical experimental results (e.g., 0.59 nm determined in Ref. [73]).

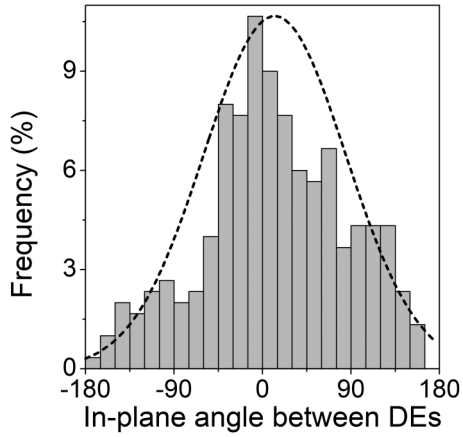

FIG. 14. Histogram of in-plane angle difference between the lower (DE1) and higher (DE2) energy dark exciton states. The dashed line is plotted assuming a normal distribution. Contrary to bright excitons, the dark excitonic lines tend to have the same polarization angle, yet with a very broad distribution. See the text for more details.

Finally, Fig. 16 shows radiative lifetimes of bright and dark excitons calculated with use of Eqs. (3) and (4). Reported lifetimes are similar for both bright excitons, hence $\tau_{BE} \approx \tau_{BE1} \approx \tau_{BE2}$ with again apparently normal-like distribution and with a mean value of 0.93 ns, thus comparable to experimentally and theoretically reported values of approximately 1 ns, and again close to typical quantum dot results [73]. Despite its simplicity, such a result warrants a comment, since the lifetime is inversely proportional to the optical activity [Eqs. (2) and (3)], thus the inverse of normal distribution on Fig. 15 will lead to (in principle quite complicated) the inverse Gaussian distribution [93] $\propto \sqrt{\frac{\lambda}{x^3}} \exp(-\frac{\lambda(x-\mu)^2}{2x\mu^2})$. However, since the bright exciton optical activity has a much larger mean value (approximately 40 Å^2) than its standard deviation (of approximately 1 Å^2), thus the inverse Gaussian distribution resembles

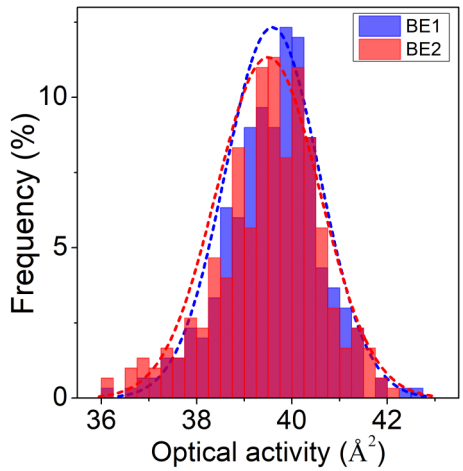

FIG. 15. Histogram of bright exciton state BE1 and BE2 optical activities, showing very similar and relatively narrow distributions. Dashed lines are plotted assuming a normal distribution. Note again that when graphs overlap, a different color is used.

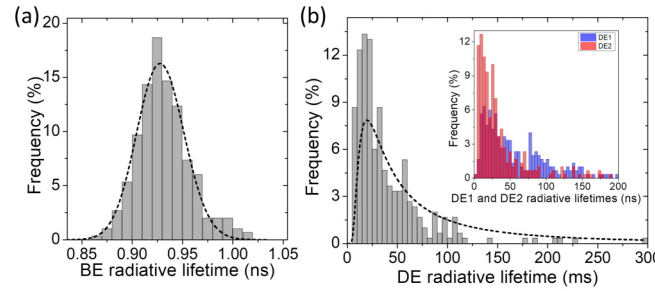

FIG. 16. Histogram of (a) bright exciton radiative lifetime, and (b) dark exciton radiative lifetime for the ensemble of alloyed quantum dots studied in this work. The inset shows the lifetime of DE1 and DE2 states separately (note that when graphs overlap, a different color is used). The dashed lines are plotted assuming a normal distribution for the bright exciton, and inverse-γ distribution for the dark exciton. See the text for more details.

a regular Gaussian distribution. A fit to this dependence is shown in Fig. 16(a) as a black dashed line, with $\lambda = 1541$ and $\mu = 0.9284$ ns, and such large λ being the reason [93] why the inverse Gaussian distribution appears very similar to the regular normal distribution.

The distribution of dark exciton lifetimes is different, with the average (mean) τ_{DE} value equal to 39 ms, and a different distribution. Since the emission intensity [Eq. (2)] and lifetimes [Eq. (3)] are inversely proportional, the weak dark exciton optical intensity, as shown earlier in Eqs. (9) and (13), corresponds to long lifetimes. Moreover, since the dark exciton optical activity resembles the exponential $\exp(-x/\langle x\rangle)$ distribution, mathematically equivalent to the γ distribution [94] with $k = 1$, then the inverse should have the distribution in the following form: $\frac{1}{x^2}\exp(-\langle x\rangle/x)$, shown as a dashed line in Fig. 16(b). Despite its oversimplicity, the inverse γ distribution describes qualitatively well the distribution of the dark exciton lifetime with no quantum dots with a lifetime below 6 ms and with a long tail of quantum dots with lifetimes reaching up to 300 ms. Such an extremely long lifetime should be taken with great care, since we consider only the radiative contribution, obtained within the tight-binding Hamiltonian and with other approximations included [65,95]. We should also note that contrary to bright excitons (and as a direct result of the differences in their optical spectra), the dark exciton states DE1 and DE2 reveal some difference of radiative lifetimes [inset of Fig. 16(b)]. Namely, the mean lifetime of the DE2 state is equal to 41 ms, whereas for DE1, including the lowest 95% cases, it is equal to 76 ms with a long tail [not shown in Fig. 16(b)] extending up to seconds (with an average of 390 ms of the 5% highest-value subset), thus corresponding to a virtually optically nonactive state, where other processes would likely dominate over radiative recombination. Since typically $\tau_{DE2} < \tau_{DE1}$, the overall DE radiative lifetime is limited by recombination through emission from DE2. Thus generally one observes that $\tau_{DE} \approx \tau_{DE2}$, which is consistent with the above-mentioned finding that in an ensemble of quantum dots considered in this work, a higher energy dark exciton state has (on average) larger optical activity for both out-of-plane and in-plane polarizations, although a sizable number of quantum dots have dominant emission through the

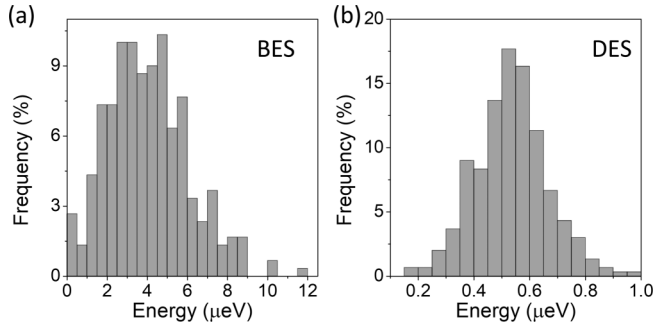

FIG. 17. Histograms of (a) the bright exciton splitting, and (b) dark exciton splitting calculated when accounting for the *s* shell only in the configuration-interaction procedure.

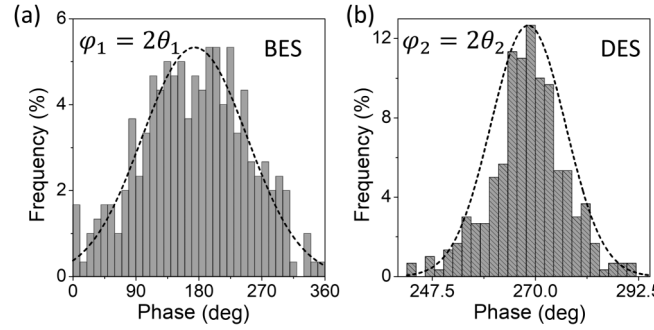

FIG. 18. Histogram of (a) $2\theta_1$ and (b) $2\theta_2$ angles using the notation of Eq. (17).

DE1 state, and a short DE1 lifetime, with a strong variation within the ensemble.

VI. SUMMARY

To summarize, changes in the local atomic arrangement in an alloyed self-assembled quantum dot can not only trigger substantial fluctuations in BES and DES, but they can also lead to a non-negligible in-plane optical activity of dark excitons. Whereas the out-of-plane emission from dark exciton states is possible for higher-symmetry C_{2v} quantum dots, and it originates from the valence-band mixing and lattice anisotropy, the in-plane emission in C_{2v} systems is forbidden by symmetry. Contrarily, in an alloyed C_1 system, dark excitons can emit in-plane polarized light. There are two contributions to this luminescence. One is related to nonvanishing matrix elements of the optical transition dipole moment, and the second is related to exchange mixing of bright and dark configurations in the configuration-interaction Hamiltonian. Dark exciton optical spectra can significantly vary in the ensemble, from nanostructures having virtually vanishing oscillator strength, to quantum dots with a substantial fraction (1/6000) of the bright exciton intensity. Our results indicate that, apart from shape-elongation and the presence of facets, alloying must be accounted for in accurate modeling of quantum dot systems used as building blocks of novel quantum devices.

ACKNOWLEDGMENTS

The author acknowledges the support from the Polish National Science Centre based on Decision No. 2018/31/B/ST3/01415. The author would like to thank Michał Gawłeczyk for reviewing the manuscript and for valuable comments.

APPENDIX A: BES and DES FOR *S*-SHELL ONLY

Whereas Fig. 3 in the main text shows BES and DES histograms for CI treatment including *s*, *p*, and *d* shells, for comparison Fig. 17 shows the (a) BES and (b) DES calculated when accounting for the *s*-shell only. In other words, Figs. 17(a) and 17(b) show histograms of δ_1 and δ_2 exchange integrals, using the notation of Eq. (6).

APPENDIX B: PHASES OF DARK AND BRIGHT EXCHANGE INTEGRALS

Figure 18 shows the histogram of exchange interaction phase θ_1 and θ_2 angles using the notation of Eq. (17). Should alloying be neglected (in the C_{2v} case), $\phi_1 = 2\theta_1$ would be equal to exactly 180°, and θ_2 to 270°, revealing a 90° phase difference between dark and bright excitons. As seen in Fig. 18, when alloying is accounted for, this relation is held approximately, with strong bright exciton phase randomization.

APPENDIX C: TWO CHANNELS OF DARK EXCITON OPTICAL ACTIVITY

For DE states, Eq. (3) for the *s*-shell case only, and in-plane (x, y) polarizations (and skipping the energy index for simplicity), takes the form

$$I^{s\text{-shell}} = \left| C_{e\downarrow,h\Uparrow} M^{x,y}_{e\downarrow,h\Uparrow} + C_{e\uparrow,h\Downarrow} M^{x,y}_{e\uparrow,h\Downarrow} + C_{e\uparrow,h\Uparrow} M^{x,y}_{e\uparrow,h\Uparrow} + C_{e\downarrow,h\Downarrow} M^{x,y}_{e\downarrow,h\Downarrow} \right|^2, \quad \text{(C1)}$$

where C's are expansion coefficients from diagonalization of the 4×4 CI Hamiltonian expressed in the *s*-shell basis.

When exchange-mixing terms are neglected ($\mathbf{H}_{\mathrm{BD}} = \mathbf{0}$), this formula is simplified with only dark exciton optical activity possible if $M^{x,y}_{e\uparrow,h\Uparrow} \neq 0$ and $M^{x,y}_{e\downarrow,h\Downarrow} \neq 0$, thus due to the nonvanishing optical dipole moment corresponding to nominally dark configurations,

$$I^{s\text{-shell}}_{\text{dipole}} = \left| C_{e\uparrow,h\Uparrow} M^{x,y}_{e\uparrow,h\Uparrow} + C_{e\downarrow,h\Downarrow} M^{x,y}_{e\downarrow,h\Downarrow} \right|^2. \quad \text{(C2)}$$

On the other hand, when exchange-mixing terms are accounted for, while in-plane optical dipole moments are neglected, i.e., $M^{x,y}_{e\uparrow,h\Uparrow} = M^{x,y}_{e\downarrow,h\Downarrow} = 0$, dark exciton optical activity is possible via an admixture of oscillator strengths from bright configurations ($C_{e\downarrow,h\Uparrow} \neq 0$ or $C_{e\uparrow,h\Downarrow} \neq 0$),

$$I^{s\text{-shell}}_{\text{exch}} = \left| C_{e\downarrow,h\Uparrow} M^{x,y}_{e\downarrow,h\Uparrow} + C_{e\uparrow,h\Downarrow} M^{x,y}_{e\uparrow,h\Downarrow} \right|^2. \quad \text{(C3)}$$

Both effects apparently play comparable roles, as discussed in the main text, and must be accounted for on an equal footing by using Eq. (C1) for the *s*-shell case only, or by using Eq. (2) when *s*, *p*, and *d* shells are accounted for.

[1] E. Poem, Y. Kodriano, C. Tradonsky, N. H. Lindner, B. D. Gerardot, P. M. Petroff, and D. Gershoni, Accessing the dark exciton with light, Nat. Phys. **6**, 993 (2010).

[2] I. Schwartz, E. R. Schmidgall, L. Gantz, D. Cogan, E. Bordo, Y. Don, M. Zielinski, and D. Gershoni, Deterministic Writing and Control of the Dark Exciton Spin Using Single Short Optical Pulses, Phys. Rev. X **5**, 011009 (2015).

[3] Y. H. Huo, V. Křápek, O. G. Schmidt, and A. Rastelli, Spontaneous brightening of dark excitons in GaAs/AlGaAs quantum dots near a cleaved facet, Phys. Rev. B **95**, 165304 (2017).

[4] R. Ohta, H. Okamoto, T. Tawara, H. Gotoh, and H. Yamaguchi, Dynamic Control of the Coupling Between Dark and Bright Excitons with Vibrational Strain, Phys. Rev. Lett. **120**, 267401 (2018).

[5] G. Sallen, B. Urbaszek, M. M. Glazov, E. L. Ivchenko, T. Kuroda, T. Mano, S. Kunz, M. Abbarchi, K. Sakoda, D. Lagarde, A. Balocchi, X. Marie, and T. Amand, Dark-Bright Mixing of Interband Transitions in Symmetric Semiconductor Quantum Dots, Phys. Rev. Lett. **107**, 166604 (2011).

[6] L. Jacak, P. Hawrylak, and A. Wojs, *Quantum Dots* (Springer, Berlin, 1998).

[7] D. Bimberg, M. Grundmann, and N. Ledentsov, *Quantum Dot Heterostructures* (Wiley, Chichester, 1999).

[8] M. Bayer, G. Ortner, O. Stern, A. Kuther, A. A. Gorbunov, A. Forchel, P. Hawrylak, S. Fafard, K. Hinzer, T. L. Reinecke, S. N. Walck, J. P. Reithmaier, F. Klopf, and F. Schäfer, Fine structure of neutral and charged excitons in self-assembled in (Ga)As/(Al)GaAs quantum dots, Phys. Rev. B **65**, 195315 (2002).

[9] I. Schwartz, D. Cogan, E. R. Schmidgall, L. Gantz, Y. Don, M. Zieliński, and D. Gershoni, Deterministic coherent writing of a long-lived semiconductor spin qubit using one ultrafast optical pulse, Phys. Rev. B **92**, 201201(R) (2015).

[10] M. Zieliński, Y. Don, and D. Gershoni, Atomistic theory of dark excitons in self-assembled quantum dots of reduced symmetry, Phys. Rev. B **91**, 085403 (2015).

[11] J. McFarlane, P. Dalgarno, B. Gerardot, R. Hadfield, R. Warburton, K. Karrai, A. Badolato, and P. Petroff, Gigahertz bandwidth electrical control over a dark exciton-based memory bit in a single quantum dot, Appl. Phys. Lett. **94**, 093113 (2009).

[12] X. Xu, B. Sun, P. R. Berman, D. G. Steel, A. S. Bracker, D. Gammon, and L. Sham, Coherent population trapping of an electron spin in a single negatively charged quantum dot, Nat. Phys. **4**, 692 (2008).

[13] P. Michler, *Quantum Dots for Quantum Information Technologies* (Springer, Cham, 2017), Vol. 237 .

[14] O. Benson, C. Santori, M. Pelton, and Y. Yamamoto, Regulated and Entangled Photons from a Single Quantum Dot, Phys. Rev. Lett. **84**, 2513 (2000).

[15] R. M. Stevenson, R. J. Young, P. Atkinson, K. Cooper, D. A. Ritchie, and A. J. Shields, A semiconductor source of triggered entangled photon pairs, Nature (London) **439**, 179 (2006).

[16] M. Prilmüller, T. Huber, M. Müller, P. Michler, G. Weihs, and A. Predojević, Hyperentanglement of Photons Emitted by a Quantum Dot, Phys. Rev. Lett. **121**, 110503 (2018).

[17] G. Bester, S. Nair, and A. Zunger, Pseudopotential calculation of the excitonic fine structure of million-atom self-assembled $In_{1-x}Ga_xAs$/GaAs quantum dots, Phys. Rev. B **67**, 161306(R) (2003).

[18] K. F. Karlsson, M. A. Dupertuis, D. Y. Oberli, E. Pelucchi, A. Rudra, P. O. Holtz, and E. Kapon, Fine structure of exciton complexes in high-symmetry quantum dots: Effects of symmetry breaking and symmetry elevation, Phys. Rev. B **81**, 161307(R) (2010).

[19] R. Singh and G. Bester, Nanowire Quantum Dots as an Ideal Source of Entangled Photon Pairs, Phys. Rev. Lett. **103**, 063601 (2009).

[20] M. A. Dupertuis, K. F. Karlsson, D. Y. Oberli, E. Pelucchi, A. Rudra, P. O. Holtz, and E. Kapon, Symmetries and the Polarized Optical Spectra of Exciton Complexes in Quantum Dots, Phys. Rev. Lett. **107**, 127403 (2011).

[21] M. Zieliński, Spectra of dark and bright excitons in alloyed nanowire quantum dots, Phys. Rev. B **100**, 045309 (2019).

[22] M. Zieliński, Excitonic fine structure of elongated InAs/InP quantum dots, Phys. Rev. B **88**, 155319 (2013).

[23] M. Zieliński, From quantum dots to quantum dashes: Excitonic spectra of highly elongated InAs/InP nanostructures, Phys. Rev. B **99**, 205402 (2019).

[24] M. Świderski and M. Zieliński, Atomistic theory of excitonic fine structure in InAs/InP nanowire quantum dot molecules, Phys. Rev. B **95**, 125407 (2017).

[25] M. Zieliński, Influence of substrate orientation on exciton fine structure splitting of InAs/InP nanowire quantum dots, Nanoscale Res. Lett. **7**, 265 (2012).

[26] M. Gawełczyk, M. Syperek, A. Maryński, P. Mrowiński, Ł. Dusanowski, K. Gawarecki, J. Misiewicz, A. Somers, J. P. Reithmaier, S. Höfling, and G. Sęk, Exciton lifetime and emission polarization dispersion in strongly in-plane asymmetric nanostructures, Phys. Rev. B **96**, 245425 (2017).

[27] M. Gawełczyk, Excitons in asymmetric nanostructures: Confinement regime, Acta Phys. Pol. A **134**, 930 (2018).

[28] P. Mrowiński, M. Zieliński, M. Świderski, J. Misiewicz, A. Somers, J. P. Reithmaier, S. Höfling, and G. Sęk, Excitonic fine structure and binding energies of excitonic complexes in single InAs quantum dashes, Phys. Rev. B **94**, 115434 (2016).

[29] M. Abbarchi, T. Kuroda, T. Mano, and K. Sakoda, Fine structure splitting reduction in droplet epitaxy GaAs quantum dots grown on (111) a surface, J. Phys. Conf. Ser. **245** 012049 (2010).

[30] A. Kors, J. P. Reithmaier, and M. Benyoucef, Telecom wavelength single quantum dots with very small excitonic fine-structure splitting, Appl. Phys. Lett. **112**, 172102 (2018).

[31] R. J. Young, R. M. Stevenson, A. J. Shields, P. Atkinson, K. Cooper, D. A. Ritchie, K. M. Groom, A. I. Tartakovskii, and M. S. Skolnick, Inversion of exciton level splitting in quantum dots, Phys. Rev. B **72**, 113305 (2005).

[32] W. Langbein, P. Borri, U. Woggon, V. Stavarache, D. Reuter, and A. D. Wieck, Control of fine-structure splitting and biexciton binding in $In_xGa_{1-x}As$ quantum dots by annealing, Phys. Rev. B **69**, 161301(R) (2004).

[33] M. T. Bjork, C. Thelander, A. Hansen, L. Jensen, M. Larsson, L. R. Wallenberg, and L. Samuelson, Few-electron quantum dots in nanowires, Nano Lett. **4**, 1621 (2004).

[34] M. T. Borgström, V. Zwiller, E. Müller, and A. Imamoglu, Optically bright quantum dots in single nanowires, Nano Lett. **5**, 1439 (2005).

[35] D. Dalacu, A. Kam, D. G. Austing, X. Wu, J. Lapointe, G. C. Aers, and P. J. Poole, Selective-area vapour–liquid–solid growth of InP nanowires, Nanotechnology **20**, 395602 (2009).

[36] D. Dalacu, K. Mnaymneh, J. Lapointe, X. Wu, P. J. Poole, G. Bulgarini, V. Zwiller, and M. E. Reimer, Ultraclean emission from InAsP quantum dots in defect-free wurtzite InP nanowires, Nano Lett. **12**, 5919 (2012).

[37] M. Bouwes Bavinck, M. Zieliński, B. J. Witek, T. Zehender, E. P. A. M. Bakkers, and V. Zwiller, Controlling a nanowire quantum dot band gap using a straining dielectric envelope, Nano Lett. **12**, 6206 (2012).

[38] S. Yanase, H. Sasakura, S. Hara, and J. Motohisa, Single-photon emission from InAsP quantum dots embedded in density-controlled InP nanowires, Jpn. J. Appl. Phys. **56**, 04CP04 (2017).

[39] G. W. Bryant, M. Zieliński, N. Malkova, J. Sims, W. Jaskólski, and J. Aizpurua, Controlling the optics of quantum dots with nanomechanical strain, Phys. Rev. B **84**, 235412 (2011).

[40] M. Świderski and M. Zieliński, Electric field tuning of excitonic fine-structure splitting in asymmetric InAs/InP nanowire quantum dot molecules, Phys. Rev. B **100**, 235417 (2019).

[41] M. Gong, W. Zhang, G.-C. Guo, and L. He, Exciton Polarization, Fine-Structure Splitting, and the Asymmetry of Quantum Dots Under Uniaxial Stress, Phys. Rev. Lett. **106**, 227401 (2011).

[42] R. Trotta, J. S. Wildmann, E. Zallo, O. G. Schmidt, and A. Rastelli, Highly entangled photons from hybrid piezoelectric-semiconductor quantum dot devices, Nano Lett. **14**, 3439 (2014).

[43] Y. Don, M. Zielinski, and D. Gershoni, The optical activity of the dark exciton, arXiv:1601.05530.

[44] S. Germanis, P. Atkinson, R. Hostein, C. Gourdon, V. Voliotis, A. Lemaître, M. Bernard, F. Margaillan, S. Majrab, and B. Eble, Dark-bright exciton coupling in asymmetric quantum dots, Phys. Rev. B **98**, 155303 (2018).

[45] S. Tomić and N. Vukmirović, Symmetry reduction in multiband hamiltonians for semiconductor quantum dots: The role of interfaces and higher energy bands, J. Appl. Phys. **110**, 053710 (2011).

[46] O. Marquardt, S. Schulz, C. Freysoldt, S. Boeck, T. Hickel, E. P. O'Reilly, and J. Neugebauer, A flexible, plane-wave based multiband k·p model, Opt. Quant. Electron. **44**, 183 (2011).

[47] R. Singh and G. Bester, Effects of atomic ordering on the electronic and optical properties of self-assembled $In_xGa_{1-x}As$/GaAs semiconductor quantum dots, Phys. Rev. B **84**, 241402(R) (2011).

[48] G. W. Bryant, N. Malkova, and J. Sims, Mechanism for controlling the exciton fine structure in quantum dots using electric fields: Manipulation of exciton orientation and exchange splitting at the atomic scale, Phys. Rev. B **88**, 161301(R) (2013).

[49] M. Zieliński, Valence band offset, strain and shape effects on confined states in self-assembled InAs/InP and InAs/GaAs quantum dots, J. Phys.: Condens. Matter **25**, 465301 (2013).

[50] P. N. Keating, Effect of invariance requirements on the elastic strain energy of crystals with application to the diamond structure, Phys. Rev. **145**, 637 (1966).

[51] R. M. Martin, Elastic properties of zns structure semiconductors, Phys. Rev. B **1**, 4005 (1970).

[52] W. Jaskólski, M. Zieliński, G. W. Bryant, and J. Aizpurua, Strain effects on the electronic structure of strongly coupled self-assembled InAs/GaAs quantum dots: Tight-binding approach, Phys. Rev. B **74**, 195339 (2006).

[53] T. Saito and Y. Arakawa, Electronic structure of piezoelectric $In_{0.2}Ga_{0.8}n$ quantum dots in gan calculated using a tight-binding method, Physica E **15**, 169 (2002).

[54] G. Bester, X. Wu, D. Vanderbilt, and A. Zunger, Importance of Second-Order Piezoelectric Effects in Zinc-Blende Semiconductors, Phys. Rev. Lett. **96**, 187602 (2006).

[55] G. Bester, A. Zunger, X. Wu, and D. Vanderbilt, Effects of linear and nonlinear piezoelectricity on the electronic properties of InAs/GaAs quantum dots, Phys. Rev. B **74**, 081305(R) (2006).

[56] A. Beya-Wakata, P.-Y. Prodhomme, and G. Bester, First- and second-order piezoelectricity in III-V semiconductors, Phys. Rev. B **84**, 195207 (2011).

[57] G. Tse, J. Pal, U. Monteverde, R. Garg, V. Haxha, M. Migliorato, and S. Tomić, Non-linear piezoelectricity in zinc blende GaAs and InAs semiconductors, J. Appl. Phys. **114**, 073515 (2013).

[58] M. A. Caro, S. Schulz, and E. P. O'Reilly, Origin of nonlinear piezoelectricity in III-V semiconductors: Internal strain and bond ionicity from hybrid-functional density functional theory, Phys. Rev. B **91**, 075203 (2015).

[59] M. Świderski and M. Zieliński, Exact diagonalization approach for atomistic calculation of piezoelectric effects in semiconductor quantum dots, Acta Phys. Pol. A **129**, (2016).

[60] J.-M. Jancu, R. Scholz, F. Beltram, and F. Bassani, Empirical spds* tight-binding calculation for cubic semiconductors: General method and material parameters, Phys. Rev. B **57**, 6493 (1998).

[61] D. J. Chadi, Spin-orbit splitting in crystalline and compositionally disordered semiconductors, Phys. Rev. B **16**, 790 (1977).

[62] M. Zieliński, Including strain in atomistic tight-binding Hamiltonians: An application to self-assembled InAs/GaAs and InAs/InP quantum dots, Phys. Rev. B **86**, 115424 (2012).

[63] S. Lee, F. Oyafuso, P. von Allmen, and G. Klimeck, Boundary conditions for the electronic structure of finite-extent embedded semiconductor nanostructures, Phys. Rev. B **69**, 045316 (2004).

[64] M. Zieliński, Multi-scale simulations of semiconductor nanostructures, Acta Phys. Pol. A **122**, 312 (2012).

[65] M. Zieliński, M. Korkusinski, and P. Hawrylak, Atomistic tight-binding theory of multiexciton complexes in a self-assembled InAs quantum dot, Phys. Rev. B **81**, 085301 (2010).

[66] J. G. Díaz, G. W. Bryant, W. Jaskólski, and M. Zieliński, Theory of InP nanocrystals under pressure, Phys. Rev. B **75**, 245433 (2007).

[67] M. S. Dresselhaus, G. Dresselhaus, and A. Jorio, *Group Theory: Application to the Physics of Condensed Matter* (Springer Science & Business Media, Springer, Hoboken, 2007).

[68] *Topics in Applied Physics*, edited by P. Michler (Springer, New York, 2003), Vol. 90.

[69] S. Lee, L. Jönsson, J. W. Wilkins, G. W. Bryant, and G. Klimeck, Electron-hole correlations in semiconductor quantum dots with tight-binding wave functions, Phys. Rev. B **63**, 195318 (2001).

[70] S. Schulz, S. Schumacher, and G. Czycholl, Tight-binding model for semiconductor quantum dots with a wurtzite crystal structure: From one-particle properties to Coulomb correlations and optical spectra, Phys. Rev. B **73**, 245327 (2006).

[71] P. T. Różański and M. Zieliński, Linear scaling approach for atomistic calculation of excitonic properties of 10-million-atom nanostructures, Phys. Rev. B **94**, 045440 (2016).

[72] P. T. Różański and M. Zieliński, Efficient computation of coulomb and exchange integrals for multi-million atom nanostructures, Comput. Phys. Commun. **238**, 254 (2019).

[73] K. Karrai and R. J. Warburton, Optical transmission and reflection spectroscopy of single quantum dots, Superlatt. Microstruct. **33**, 311 (2003).

[74] G. A. Narvaez, G. Bester, and A. Zunger, Excitons, biexcitons, and trions in self-assembled (In,Ga)As/GaAs quantum dots: Recombination energies, polarization, and radiative lifetimes versus dot height, Phys. Rev. B **72**, 245318 (2005).

[75] E. L. de Oliveira, E. L. Albuquerque, J. S. de Sousa, G. A. Farias, and F. M. Peeters, Configuration-interaction excitonic absorption in small Si/Ge and Ge/Si core/shell nanocrystals, J. Phys. Chem. C **116**, 4399 (2012).

[76] C. Dion, P. Desjardins, N. Shtinkov, M. D. Robertson, F. Schiettekatte, P. J. Poole, and S. Raymond, Intermixing during growth of InAs self-assembled quantum dots in InP: A photoluminescence and tight-binding investigation, Phys. Rev. B **77**, 075338 (2008).

[77] W. Sheng and S. J. Xu, Optical characterization of structure for semiconductor quantum dots, Phys. Rev. B **77**, 113305 (2008).

[78] T. Warming, E. Siebert, A. Schliwa, E. Stock, R. Zimmermann, and D. Bimberg, Hole-hole and electron-hole exchange interactions in single InAs/GaAs quantum dots, Phys. Rev. B **79**, 125316 (2009).

[79] N. Liu, J. Tersoff, O. Baklenov, A. L. Holmes, and C. K. Shih, Nonuniform Composition Profile in $In_{0.5}Ga_{0.5}As$ Alloy Quantum Dots, Phys. Rev. Lett. **84**, 334 (2000).

[80] A. J. Williamson, L. W. Wang, and A. Zunger, Theoretical interpretation of the experimental electronic structure of lens-shaped self-assembled InAs/GaAs quantum dots, Phys. Rev. B **62**, 12963 (2000).

[81] I. Vurgaftman, J. á. Meyer, and L. á. Ram-Mohan, Band parameters for III–V compound semiconductors and their alloys, J. Appl. Phys. **89**, 5815 (2001).

[82] E. Ivchenko, *Optical Spectroscopy of Semiconductor Nanostructures*, 2nd ed. (Alpha Science, 2005).

[83] E. Tsitsishvili, Impact of heavy hole–light hole coupling on the exciton fine structure in quantum dots, Physica E **87**, 161 (2017).

[84] R. Singh and G. Bester, Lower Bound for the Excitonic Fine Structure Splitting in Self-Assembled Quantum Dots, Phys. Rev. Lett. **104**, 196803 (2010).

[85] M. Zieliński, Vanishing fine structure splitting in highly asymmetric InAs/InP quantum dots without wetting layer, Sci. Rep. **10**, 13542 (2020).

[86] M. Gong, B. Hofer, E. Zallo, R. Trotta, J.-W. Luo, O. G. Schmidt, and C. Zhang, Statistical properties of exciton fine structure splitting and polarization angles in quantum dot ensembles, Phys. Rev. B **89**, 205312 (2014).

[87] T. Heindel, A. Thoma, I. Schwartz, E. R. Schmidgall, L. Gantz, D. Cogan, M. Strauß, P. Schnauber, M. Gschrey, J.-H. Schulze *et al.*, Accessing the dark exciton spin in deterministic quantum-dot microlenses, Apl Photon. **2**, 121303 (2017).

[88] R. Wojnar, Rayleigh's distribution, wigner's surmise and equation of the diffusion, Acta Phys. Pol. A **123**, 624 (2013).

[89] M. L. Mehta, *Random Matrices* (Elsevier, Amsterdam, 2004).

[90] C. Tonin, R. Hostein, V. Voliotis, R. Grousson, A. Lemaitre, and A. Martinez, Polarization properties of excitonic qubits in single self-assembled quantum dots, Phys. Rev. B **85**, 155303 (2012).

[91] Y. Léger, L. Besombes, L. Maingault, and H. Mariette, Valence-band mixing in neutral, charged, and Mn-doped self-assembled quantum dots, Phys. Rev. B **76**, 045331 (2007).

[92] T. Smoleński, T. Kazimierczuk, M. Goryca, T. Jakubczyk, Ł. Kłopotowski, Ł. Cywński, P. Wojnar, A. Golnik, and P. Kossacki, In-plane radiative recombination channel of a dark exciton in self-assembled quantum dots, Phys. Rev. B **86**, 241305(R) (2012).

[93] R. Chhikara, *The Inverse Gaussian Distribution: Theory: Methodology, and Applications* (CRC, Boca Raton, FL, 1988).

[94] A. Papoulis, *Random Variables and Stochastic Processes* (McGraw-Hill, New York, 1965).

[95] W.-d. Sheng, M. Korkusinski, A. D. Güçlü, M. Zielinski, P. Potasz, E. S. Kadantsev, O. Voznyy, and P. Hawrylak, Electronic and optical properties of semiconductor and graphene quantum dots, Front. Phys. **7**, 328 (2012).